EasyChair Preprint

№ 1292

Effects of Turning Radius on Skid-Steered Wheeled Robot Power Consumption on Loose Soil

Jean-Sebastien Fiset, Meysam Effati and Krzysztof Skonieczny

July 15, 2019

Effects of Turning Radius on Skid-Steered Wheeled Robot Power Consumption on Loose Soil

Jean-Sebastien Fiset, Meysam Effati, and Krzysztof Skonieczny

Abstract This paper highlights the need for a new power model for skid-steered wheeled robots driving on loose soil, and lays the groundwork to develop such a model. State-of-the-art power modeling assumes hard ground; under typical assumptions this predicts constant power consumption over a range of small turning radii where the inner wheels are rotating backwards. However, experimental results performed both in the field and in a controlled laboratory show that, on sand, power is not in fact constant with respect to turning radius in this case. Power peaks in a newly identified range of turns where the inner wheels rotate backwards but are being dragged forward. Data shows higher motor torque and wheel sinkage in this range. A skidding wheel that is sunk into loose soil bulldozes a pile of sand; initial modeling of this phenomena reproduces the trend in additional power with respect to turning radius. As work on a full power model for loose soil continues, this work identifies turning radii to avoid whenever possible in practice.

1 Introduction

Skid-steered rovers use different velocities for the left and right wheels to maneuver. Due to their mechanical simplicity, maneuverability and robustness, they are widely used for excavation, construction, military, and planetary exploration applications. Energy-efficient motion is important for any of these applications, especially when planning paths in power-starved environments. However, the power consumption for skid-steered rovers can be high, and also highly variable, compared to other steering mechanisms (such as explicit or Ackerman steering) due to the lateral motion resistance while skidding in a turn. Detailed power modeling is thus essential for

Jean-Sebastien Fiset, Meysam Effati, and Krzysztof Skonieczny
Department of Electrical and Computer Engineering, Concordia University, Montreal, QC, Canada, e-mail: e-mail:j_fise@encs.concordia.ca, m_effati@encs.concordia.ca, kskoniec@encs.concordia.ca

(a) (b)

Fig. 1 a) Clearpath Husky A200 on the dunes of the White Sands National Monument. b) Argo J5 at the Canadian Space Agency Mars analogue terrain

this popular class of mobile robots. Although loose soil is frequently encountered in the applications cited above, skid-steered rover power consumption on loose soil has not yet received much attention in the literature.

Preliminary work revealed that the shortest distance path (where the skid-steered wheeled robot performs a point turn, i.e. turn in place using equal and opposite wheel rotations, followed by a straight line and a second point turn) is not the most energy efficient path on loose soil. This is shown with experimental data collected with two skid-steered wheeled robots showing a significant reduction in energy consumption when replacing the point turn segments with larger radius turns. These field tests were conducted at White Sands National Monument (Fig. 1a) and at the Canadian Space Agency (CSA) Mars analogue terrain (Fig. 1b). Even though this preliminary work focused only on the energy consumption of skid-steered rovers, it further highlights the need for a power model specific to this type of rover on loose soil, with the goal of computing energy-efficient paths.

The state-of-the-art in power modeling for skid-steered rovers is for motion on rigid terrain. One such established class of models is based on instantaneous centers of rotation (ICR) that are estimated online without prior knowledge of terrain properties [1]. The ICR correspond to the degree of skidding by the rover. Given ICR, the work of [2] (and followed by [3]) uses the kinematic model for tracked mobile robots found in [4][5] to successfully model power on a rigid terrain. An expanded version of this power model considering terrain elevation was used with a Sample Based Model Predictive Optimization (SBMPO) scheme to find energy-efficient paths [6] on asphalt and grass. It has also been used by the authors in [7] to optimize the energy consumption of a skid-steered rover on rigid terrain by explicitly considering the radii of the circular arcs along its path.

A recent physics-based power model [8] focuses on friction, the location of the center of mass, the turning radius and the terrain relief. Their research focused on hard surfaces and the quality of the fit decreased when roving on grass. The work presented in [9] used the dynamic model of skid-steered rovers provided in [10][11] to model the power consumption.

The contributions of this work are: (1) empirically showing shortcomings of existing power models, and discovering a special operating case (wheels dragged against their own rotation) corresponding to where the discrepancy is greatest; (2)

isolating significantly higher motor torque and wheel sinkage in controlled experiments replicating the above special case; and (3) linking trends in increased sinkage to higher rover power consumption in promising preliminary modeling.

The remainder of the paper is structured as follows. Section 2 describes the kinematics of a skid-steered wheeled robots and a simplified ICR-based power model along with its predictions. Section 3 provides an overview of the equipment used in this research and Section 4 shows the results of the tests performed. Finally, Section 5 summarizes the conclusions, future work, and pratical lessons learned.

2 Power Modeling of Skid-Steered Wheeled Robots

The work of [12] shows that, on hard flat ground, a skid-steered rover's turning radius is inversely related to required torque and thus power consumption. Accordingly, this power modeling analysis explicitly considers turning radius. This section summarizes existing work on the kinematics of skid-steered wheeled robots and their power modeling when considering slip, on flat ground.

2.1 Kinematic Model

For differential wheeled and tracked vehicles, the location of the center of rotation for the vehicle, ICR_v, is not the same as the center of rotation of each wheel or track set [4], as it can be seen in Fig. 2a. Due to slippage, these instantaneous centers of rotation (ICR) lie outside of the wheels and they are expressed with respect to the vehicle's coordinate frame such that $ICR_l = (x_{ICR_l}, y_{ICR_l})$ and $ICR_r = (x_{ICR_r}, y_{ICR_r})$. As stated by the Kennedy-Aronholdt theorem, the vehicle's center of rotation as well as the two ICRs are located on the same line, parallel to the vehicle X axis.

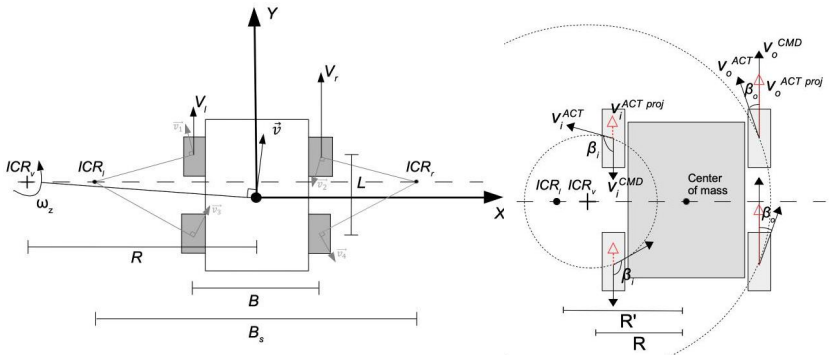

(a) (b)

Fig. 2 a) Schematic figure of a 4-wheel skid-steered wheeled robot. b) Schematic figure of a four-wheel skid-steered rover performing a turn of radius $B/2 < R < R'$. For the inner wheels, the projection of tangential velocity (or actual velocity of the wheel v^{ACT}) is opposite to the commanded wheel velocity v^{CMD}.

The distance from the geometric center of the rover to this parallel line is y_{ICR_v} such that $y_{ICR_v} = y_{ICR_l} = y_{ICR_r}$. The position of the left and right instantaneous centers of rotation as a function of the robot's linear velocities (v_x and v_y), angular velocity ω_z and commanded left and right wheels velocities (V_l and V_r respectively; note that these are the control inputs) is reported in the work of [4].

It should be to noted that the location of the center of mass has an impact on the location of the left and right instantaneous centers of rotation. As it moves closer to one side of the vehicle, the wheels on this side will slip less, thus resulting in an instantaneous center of rotation closer to those wheels [4].

In this work, the distance between the two centers of rotation is defined as the slip track (B_s).

$$B_s = x_{ICR_r} - x_{ICR_l} \tag{1}$$

As the ICRs always lie outside of the rover's track due to slippage, the slip track is always greater that the track width, i.e. $B_s \geq B$ [4][5]. This was validated for both platforms tested (Clearpath Husky and Argo J5), which suggests a generality in the results presented in this work. It is also important to note that, even if R (or x_{ICR_v}) vary within $\pm\infty$, the values of x_{ICR_l}, x_{ICR_r} and y_{ICR_v} remain within bounded areas for a specific terrain, regardless of the maneuver [4][5]. Hence, the slip track can be used as a measure of the overall skidding of the wheeled vehicle. A bigger slip track indicates a higher overall skidding, as the amount wheel velocity contributing to the lateral motion is increased and the amount of wheel velocity contributing to longitudinal displacement is decreased. Accordingly, the ICR positions can help characterize the properties of a terrain [5]. Studies have also shown that knowing the instantaneous center of rotation locations can enhance the pose estimation [1][4] and be used for power modeling [2][3][6].

The following equations are used to express the linear and angular velocity in the body frame when considering slippage.

$$v_y = \frac{V_l x_{ICR_r} - V_r x_{ICR_l}}{B_s} \quad (2) \qquad v_x = \frac{(V_r - V_l) y_{ICR_v}}{B_s} \quad (3) \qquad \omega_z = \frac{V_r - V_l}{B_s} \quad (4)$$

If it is assumed that the left and right instantaneous centers of rotation are symmetric (i.e. $x_{ICR_l} = -x_{ICR_r}$) and that the ICR lie directly on the X-axis, Eq. 2 and 3 can be simplified to:

$$v_y = \frac{V_r + V_l}{2}, \tag{5}$$

$$v_x = 0. \tag{6}$$

If v_y is tangential to the rotation, then it is known that

$$v_y = \omega_z R, \tag{7}$$

where R is the turning radius of the robot, depicted in Fig. 2a. Accordingly, the turning radius R can be defined as a function of V_r, V_l and B_s.

$$R = \frac{B_s}{2}\left(\frac{V_r + V_l}{V_r - V_l}\right) \tag{8}$$

In this paper, R' is defined as the turning radius at which the inner wheels are not commanded to turn. Using Eq. 8, the value of R' for a left turn (i.e when $V_l = 0$) can be found with the following equation:

$$R' = \frac{B_s}{2}. \tag{9}$$

The first assumption made in this work is that the total absolute velocity v_c of the rover is constant. This total absolute velocity is defined as

$$v_c = \frac{|V_r| + |V_l|}{2}. \tag{10}$$

This assumption is more realistic for skid-steered rovers than a constant forward velocity (v_y) assumption, for example. As turning radius approaches zero, constant forward velocity would require angular velocity, and V_l and V_r, to approach infinity. In real systems, motors producing V_l and V_r saturate at a maximum value. Thus, the stated assumption is more realistic than one of constant forward velocity.

Note that for $R \geq R'$, V_r and V_l are both positive, and thus the constant v_c assumption is equal to constant forward velocity (Eq. 5). For $R < R'$, on the other hand, V_r and V_l are of opposite sign, thus the constant v_c assumption is equal to constant angular velocity (Eq. 4). Therefore, the angular velocity of the robot can be rewritten as a function of v_c, using Eq. 4, 5, 7, and 10.

$$\omega_z = \begin{cases} \frac{2v_c}{B_s} & \text{if } 0 \leq R < R' \\ \frac{v_c}{R} & \text{if } R \geq R' \end{cases} \tag{11}$$

2.1.1 Special Case (when $B/2 < R < R'$)

A further analysis of the skid-steered wheeled robot kinematics, when considering the slip track B_s, led to studying a particular set of turning radii. When the rover is moving along a circular arc path with a radius that is slightly bigger than half of its width ($B/2$) but smaller than R', the inner wheels are rotating backward but are actually being dragged forward by the outer wheels. Fig. 2b shows the actual and commanded velocity vectors of the inner wheel (v_i^{ACT} and v_i^{CMD} respectively) when the rover is dealing with this set of turns. If the slip angle β is defined as being the angle between v^{CMD} and v^{ACT}, the inner wheels' slip angle (β_i) in this special case will always be greater than 90°. The presence of a slip angle is specific to skid-steered wheeled robots as the wheels are fixed and lateral movement is required to achieve arc paths.

It should be noted that, going forward, the experiments are done with left hand turns, such that $V_l = v_i^{CMD}$ and $V_r = v_o^{CMD}$. The power consumption and the inner wheel sinkage during a left hand turn with a radius in the special case range will be presented and discussed in Section 4.

2.2 Power Model

As mentioned earlier, there is a lack of power modeling for skid-steering of loose soil; instead the state-of-the-art is for rigid terrain. On rigid ground, the dynamic friction between the wheels that causes the vehicle to slip during a turn can be modeled using the known ICR-based power model. Based on the work of [2][3], the power loss of a skid-steered rover can be modeled as

$$P = \mu|\omega_z| \sum_{n=1}^{N} p_n \|\mathbf{a} - \mathbf{C_n}\| + G(|V_r| + |V_l|), \tag{12}$$

where μ is the friction coefficient, ω_z is the angular velocity, p_n is the normal force, $\|\mathbf{a} - \mathbf{C_n}\|$ is the distance between the nth wheel and its respective ICR and G is the internal rolling resistance coefficient due to wheel and soil deformation, but also due to internal resistance from the gear and driving belt.

In this paper, it is assumed that the rover is symmetric and operating on flat ground, causing the normal forces and the distances $d_{ICR} = \|\mathbf{a} - \mathbf{C_n}\|$ to be equal and constant for all wheels. Under these assumptions, and using Eq. 11, the power model can be simplified to

$$P = \begin{cases} \frac{2c_1}{B_s} + c_2 & \text{if } 0 \leq R < R' \\ \frac{c_1}{R} + c_2 & \text{if } R \geq R' \end{cases} \tag{13}$$

where c_1 and c_2 are constants and defined as follow:

$$c_1 = \mu v_c m g d_{ICR}, \tag{14}$$

$$c_2 = 2G v_c, \tag{15}$$

where m is the mass of the rover, g is the gravitational constant, and d_{ICR} is the distance between a wheel and its instantaneous center of rotation.

As it can be seen in Eq. 13 and illustrated in Fig. 3, when operating on flat ground under a constant v_c, it is noted that the modeled power remains constant for turning radii smaller than R'. It will be shown in Section 4.1 that this prediction is inconsistent with observed results on loose sandy soil.

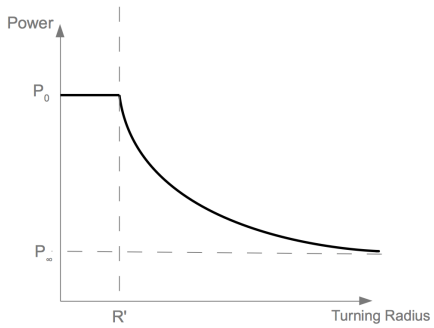

Fig. 3 Predicting power vs. turning radius using Eq. 13 on flat ground. Comparison with the experimental results (Fig. 6a) shows the limitation of the approach.

3 Test Equipment and Setup

For the purpose of this research, a popular skid-steered wheeled robot is used to show the limitations of the existing power model on sand. To further analyze the wheel-soil interaction of the inner wheels for the special case identified (i.e. when $B/2 < R < R'$), a single-wheel test bed is used.

(a)

Parameter	Value
Track Width (B)	0.545 m
Defined Slip Track (B_s)	1.1 m
Length (L)	0.52 m
Wheel radius (r)	0.165 m
Mass (m)	63 kg

(b)

Fig. 4 a) Clearpath Husky A200 platform mounted with a landmark prism (for position tracking), an IMU and an additional box of sand to place the center of mass of the rover at its centroid. b) Table of geometric parameters for the Clearpath Husky A200

It should be noted that, in the laboratory sandbox, the GRC-1 simulant [13] is used to replicate lunar and martian soil. To limit the soil disturbance to improve repeatability, the soil is prepared by loosening it with shovels, compacting it with a tamper and then leveling it with rakes. This procedure is thoroughly explained in [14]. The sand at the CSA Mars analogue terrain is less characterized but cone penetrometer measurements confirmed that the sand had a significantly higher density.

3.1 Clearpath Husky A200

The platform used to experimentally validate the existing power model is the Clearpath Husky A200. This medium-sized skid-steered wheeled robot is fully supported in ROS. Although this rover has a built-in power measurement system, our preliminary testing unveiled some inaccuracy in the current measurements. An external board using the Texas Instruments INA226 bidirectional current and power sensor is therefore designed and implemented to measure the current and voltage drawn by the left and right motor controllers and publish the data to a ROS topic. The orientation of the robot is recorded using the VectorNav VN-100R rugged inertial measurement unit (IMU). The left and right wheels' commanded velocities are also recorded from the built-in ROS controller. For the purpose of our testing, an additional weight of 8 kg is placed at the front of the robot to align the center of mass with the geometric center (as shown in Fig. 4a). The equal distribution of the

weight ($\pm 0.5\%$) on all four wheels was verified using the Computerscales Accuset II portable car scale.

The Husky A200 is used at the CSA Mars analogue terrain (Fig. 1b) and the power consumption of the brushed DC motors is measured for a set of turns of radii close to R', with $v_c = 0.3$ m/s. These tests are also repeated in a 2.2×2.2 m sandbox and the results of these two test campaigns are explained in Section 4.1 and 4.2.

3.2 Five-Axis Single-Wheel Test Bed

Fig. 5a shows the five-axis single-wheel test bed used for this research. The position of the wheel unit along the X^S and Y^S axis and its orientation around the Z^S axis can be controlled while the wheel unit is free to move along Z^S. The wheel axis is driven by a Maxon RE35 motor and MaxPos 50/5 driver. The load applied to the wheel is set to $1/4$ of the Husky weight by using a counterweight and the sinkage is measured using a linear potentiometer. The ATI Delta IP60 six-axis force/torque sensor is also mounted between the wheel unit and the wheel itself.

This setup was used to reproduce the circular arc motion of an inner wheel during a set a turns of radii in and around the $B/2 < R < R'$ range. Using the data collected during the Husky tests in the sandbox, the wheel axis was first rotated by β before launching the test program. This program used the desired v^{CMD} and v^{ACT} velocities to set the wheel angular velocity and the tangential velocity, respectively. Knowing the rover geometry, the inner wheel's motion radius R_i is computed using the desired turning radius of the rover (R) and the angular velocity around Z^S can be calculated knowing v^{ACT} and R_i. The results of these tests are presented in Section 4.3.

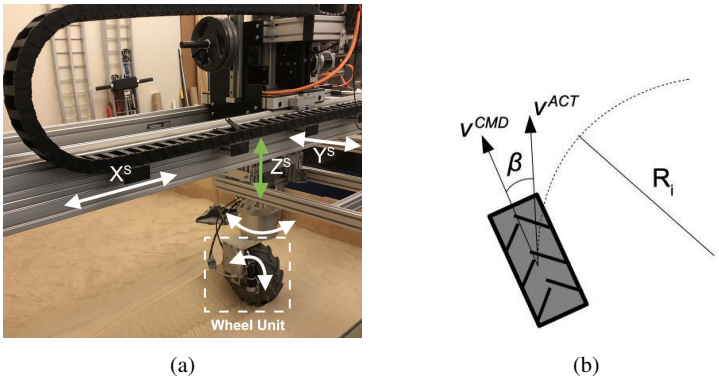

(a) (b)

Fig. 5 a) A Husky wheel placed in the single-wheel test bed. b) A Husky wheel performing a circular arc path of radius R_i with a commanded linear velocity v^{CMD}, a tangential velocity v^{ACT}, and a slip angle β.

4 Results

Experimentally measured power consumption by the Husky on loose soil shows important discrepancies compared to the model for hard terrain presented in Eq. 12. Further analysis of experimental data exposes two possible contributing factors causing the increase in power consumption below R': motor torque and wheel sinkage. A particular focus is put on the inner wheels for the special case identified, i.e when they are rotating backwards but being dragged forward by the outer wheels.

4.1 Power Model For Hard Ground Limitation on Loose Soil

The purpose of these first tests is to experimentally validate that the power consumption of a skid-steered wheeled robot is not constant below R'. In order to demonstrate this, 90° turns of radii around $R' = 0.55$ m are executed with the Clearpath Husky A200 platform. The average power measured during these maneuvers is depicted in Fig. 6a. In this figure, the results recorded at CSA are compared with the results from the controlled sandbox tests. It is clear that the power doesn't remain constant for turns where the inner wheels are rotating backwards as we see the power consumption rise significantly (to values 25% to 30% higher than $P(R')$) and peak in the special case region region identified in Section 2.1, i.e. when the center of rotation lies between the inner wheels and their ICR ($B/2 < R < R'$). It should be noted that the same trend was observed with two other constant v_c values.

Fig. 6b depicts the power consumption with respect to time for the set of turns performed in the GRC-1 soil bed. It should be noted that the total power consumption of the left and right motor drivers is increasing with time in the case of maneuvers with $R \leq R'$. Another important observation is that the time to complete the 90° rotation increases as R approaches R'. This is most likely due to the fact that the rover needs to overcome a higher resistance force, in particular when the inner

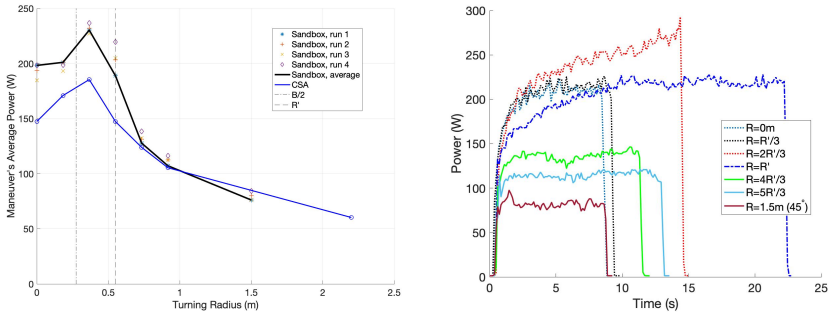

(a) (b)

Fig. 6 a) Average power consumed during a set of 90° turns performed in the laboratory's sandbox and at the CSA Mars analogue terrain (in green), showing non-constant P for $0 \leq R \leq R'$ (contrast with Fig. 3). b) Power consumed over time for a set of turns performed in the controlled laboratory sandbox. For $R \leq R'$ (dotted lines), power rises as the turn progresses.

wheels are fixed and not excavating the soil (at R'). It should also be noted that similar results were observed when repeating this set of tests at the CSA Mars analogue terrain with another skid-steered wheeled robot, the Argo J5.

4.2 Torque-Proportional Curve

For any electromechanical system, the input electrical power P equals the output mechanical power P_{out} such that $P = \eta P_{out} = \eta\tau\omega$, where η is the power efficiency factor, τ is the output torque and ω is the angular velocity of the wheel in this case. Assuming a constant efficiency, the measurements gathered in the set of 90° turns can be used to draw a torque-proportional curve knowing the following:

$$\tau \propto \frac{P}{\omega}. \tag{16}$$

Fig. 7 shows the inner and outer wheels torque-proportional curve using the power measurements and the commanded angular velocity (ω^{CMD}). For the $2R'/3$ case, which corresponds to the turning radius in the special case range presented in Section 2.1.1, the inner wheels' torque is clearly isolated as it requires around 70% more torque for these wheels to rotate versus the $R'/3$ case.

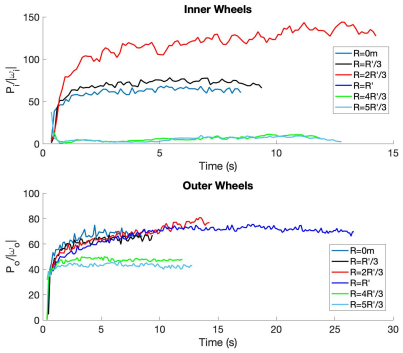

Fig. 7 Inner (top) and outer (bottom) wheels torque-proportional curve following Eq. 16. For the inner wheels, the $2R'/3$ case significantly needs more torque than the other radii in order to achieve its desired turn.

The significant increase in measured torque for special case turns, i.e. the $2R'/3$ case, is most likely due to the fact that the grousers need to excavate the sand in front of the forward displacement of the inner wheels. As the wheel progresses and pushes the sand pile, it becomes harder for the grousers to excavate sand from under the wheel to the front, hence requiring more torque to rotate the wheel. A one-dimension schematic comparison of a normal sand excavation process (when the wheel moves out of the region where sand was excavated) and a scenario when the sand is being compacted in front of the wheel is depicted in Fig. 8. As more torque is required by the motor to rotate the wheel, the system needs to consume an additional amount of electrical power. Therefore, a first argument to explain the peak in power consumption shown in Fig. 6a is identified.

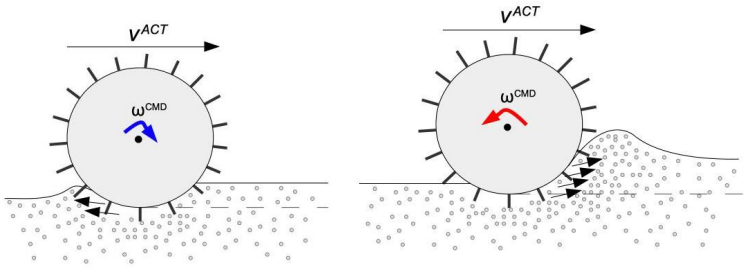

(a) (b)

Fig. 8 Schematic comparison of a) the usual excavation process by the wheel angular rotation (ω^{CMD}) is aligned with the wheel progression (v^{ACT}), i.e. when $\beta = 0°$, and (b) the excavation process when the wheel rotation is opposite to the wheel progression, i.e. when $\beta = 180°$.

4.3 Sinkage

Further tests using the five-axis single-wheel test bed are executed to investigate the sinkage of the Husky's inner wheels by reproducing their motion during a turn of radius R. Table 1 presents the inner wheel's turning radius (R_i), slip angle β, tangential velocity (v^{ACT}) and commanded wheel linear velocity (v^{CMD}) used to replicate an inner wheel trajectory for each turning radius R tested.

Table 1 Parameters to reproduce the Husky's inner wheel trajectories tested

R	R_i	β	v^{ACT}	v^{CMD}
$R'/3$	0.141 m	60°	0.057 m/s	0.17 m/s
$2R'/3$	0.267 m	100°	0.042 m/s	0.08m/s
R'	0.613 m	40°	0.05 m/s	0 m/s
$4R'/3$	0.795 m	25°	0.127 m/s	0.07m/s

The sinkage measured by the linear potentiometer for the four test cases is reported in Fig. 9. The first observation that should be made is that the wheel sinks more when $R \leq R'$ than for the $4R'/3$ case, which is consistent with the discrepancies observed between the power model and experimental results as the model doesn't take into account the effects of loose terrain. For skid-steered wheeled robots, maneuvering on loose soil means that the wheels sink as they are slipping and skidding. This requires a higher power consumption in order to push the sand accumulated next to the wheels and, as observed in Section 4.1, this increase is more significant below R'.

It should also be noted that for the $2R'/3$ turn, the sinkage is greater than in the $R'/3$ turn, even if the wheel is rotating more than twice faster in the latter case. This

additional sinkage means that there is also an additional amount of sand accumulation next to the inner wheels, which results in an increasing power required not only to drag the inner wheels but also to bulldoze the sand pile next to the wheels.

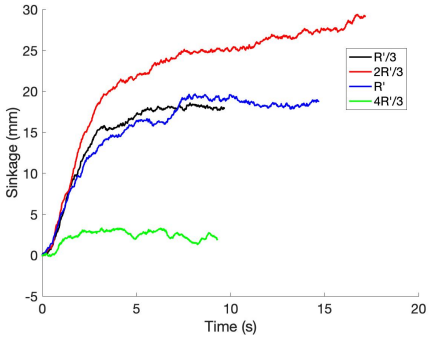

Fig. 9 Measured sinkage versus time for the set of turning radii tested (Table 1). The wheel sinks more in the $2R'/3$ case than in the $R'/3$ even if its rotation speed is less than half.

Other measurements recorded during the single-wheel tests yielded no additional insights on the contributing factors increasing the power required to achieve a circular arc path of radii smaller than R'.

4.4 Sand Bulldozing Force (F^{SB})

Wheel sinkage is essential to properly estimate the bulldozing force required to push the sand accumulation next to the wheels. By simplifying the Skonieczny algorithm presented in [16] to model the excavation force throughout a wide-blade tool cut using the GRC-1 soil properties and a few assumptions, the inner wheels' sand bulldozing force can be estimated using the sinkage measurements reported in Section 4.3. Fig. 10 shows the results of this novel modeling of the inner wheels bulldozing forces (F_i^{SB}) that the rover needs to overcome in order to achieve its desired turn. The modeled force stabilizes when the sand pile reach its estimated maximum height, which is a function of the repose angle, slip angle, and steady state sinkage.

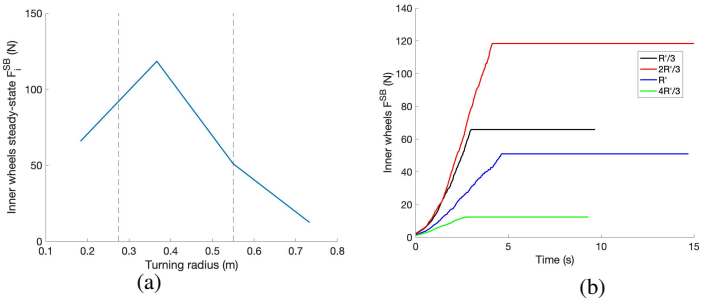

Fig. 10 a) Steady-state value of the inner wheels' sand bulldozing force (F_i^{SB}) versus turning radius. The force peaks at $2R'/3$ like the average power measured shown in Fig. 6a. b) Sand bulldozing force over time for the set of turns tested.

Even as further improvements are currently being applied to the model, these two figures show encouraging results as the steady state value of the sand bulldozing force (Fig. 10a) depicts the same trend as the power consumption measurements presented in Fig. 6a. The evolution of the force with respect to time for the set of turns tested also replicates the results of Fig. 6b although the modeled force reach a steady state value faster that the experimental results. F_i^{SB} is slightly bigger for $R'/3$ compared to R' (even though these two tests recorded similar sinkage) because the slip angle (β) of $R'/3$ is greater than the slip angle of R'. The projection of the wheel perpendicular to the motion increases as β increases, thus resulting in a higher modeled sand pile accumulation and higher bulldozing force.

5 Conclusion, Future Work, and Practical Lessons Learned

A key contribution of this work is the identification of a special case in the power consumption of skid-steered wheeled robots. When the turning radius is slightly bigger than half of the width of the rover but smaller than the turning radius where $v_i^{CMD} = 0$, i.e. $B/2 < R < R'$, measured power consumption is significantly higher than existing models predict. As shown in Fig. 6, this special case has an average power consumption approximately 20% higher than for a point turn, and it exhibits the highest rise in instantaneous power with respect to time. Two arguments to explain the increasing power consumption of this special case are studied in this work. First, since the inner wheels' rotation is opposite to their forward progression, i.e. $\beta > 90^\circ$ (as they are being dragged by the other wheels, which is intuitively an inefficient way of driving), additional motor torque is required to excavate the sand in a dense area, hence requiring additional power. The second contributing factor comes from the fact that, for this set of turns, the rover experiences more sinkage (in particular for the inner wheels) and this additional sinkage results in a higher bulldozing force required to push the sand accumulated next to the wheels. Even though the results shown in this paper are specific to the Clearpath Husky platform, the fact that $B_s > B$ for all skid-steered wheeled robots suggests that the trend in the results can be generalized. On the other hand, the magnitude of the results is specific to the platform and soil used.

Future work will model the amount of torque required for the grousers to excavate the sand in a compacted area when $\beta > 90^\circ$. Additional work should also be made in order to predict the sinkage of all of the skid-steered rover's wheels to successfully predict the power required to apply the sand bulldozing force.

Even before a power model is developed to fully account for the contributing factors of increased power listed above, a practical lesson learned in this work is to avoid turns of radii $B/2 < R < R'$ whenever possible when designing an energy-efficient path for skid-steered wheeled vehicles on loose soil. [0]

Acknowledgements The authors acknowledge financial support from the Natural Sciences and Engineering Research Council of Canada (NSERC), funding and collaboration from Mission Control Space Services Inc., and thank the CSA for facilitating access to their Mars analogue terrain.

References

1. J.Pentzer, S. Brennan, and K. Reichard, "Model-based Prediction of Skid-steer Robot Kinematics Using Online Estimation of Track Instantaneous Centers of Rotation", *Journal of Field Robotics*, Vol. 31, No. 3, March, 2014, pp. 455-476.
2. J. Morales, J. L. Martinez, A. Mandow, A. J. Garcia-Cerezo, and S. Pedraza, "Power Consumption Modeling of Skid-steer Tracked Mobile Robots on Rigid Terrain", *IEEE Transactions on Robotics*, Vol 25, No. 5, 2009, pp. 1098-1108.
3. J. Pentzer, S. Brennan, and K. Reichard, "On-Line Estimation of Vehicle Motion and Power Model Parameters for Skid-Steer Robot Energy Use Prediction", *American Control Conference (ACC)*, June 2014, Portland, Oregon, USA, pp. 2786-2791.
4. J. L. Martinez, A. Mandow, J. Morales, S. Pedraza, A. J. Garcia- Cerezo, "Approximating kinematics for tracked mobile robots", *The International Journal of Robotics Research*, Vol. 24, No. 10, October, 2005, pp. 867-878.
5. G. Reina, and R. Galati, "Slip-based terrain estimation with a skid-steer vehicle", *Vehicle System Dynamics*, Vol. 54, No. 10, 2016, pp. 1384-1404.
6. J. Pentzer, K. Reichard, and S. Brennan, "Energy-based path planning for skid-steer vehicles operating in areas with mixed surface types", *American Control Conference (ACC)*, July 2016, Boston, MA, USA, pp. 2110-2115.
7. M. Effati and K. Skonieczny, "Circular Arc-Based Optimal Path Planning for Skid-Steer Rovers", *IEE Canadian Conference on Electrical Computer Engineering (CCECE)*, May 2018, Quebec, QC, Canada.
8. S. Dogru, and L. Marques, "A Physics-Based Power Model for Skid-Steered Wheeled Mobile Robots", *IEEE Transactions on Robotics*, Vol. 34, No. 2, April, 2018, pp. 421-433.
9. N. Gupta, C. Ordonez, and E. G. Collins, "Dynamically feasible, energy efficient motion planning for skid-steered vehicles", *Autonomous Robots*, Vol. 41, No. 2, 2017, pp. 453-471.
10. W. Yu, O. Chuy, E. G. Collin, and P. Hollis, "Analysis and Experimental Verification for Dynamic Modeling of A Skid-Steered Wheeled Vehicle", *IEEE Transactions on Robotics*, Vol. 26, No. 2, April, 2010, pp. 340353.
11. C. Ordonez, N. Gupta, B. Reese, N. Seegmiller, A. Kelly, and E. G. Collins "Learning of skid-steered kinematic and dynamic models for motion planning", *Robotics and Autonomous Systems*, Vol. 95, 2017, pp. 207-221.
12. B. Shamah, "Experimental Comparison of Skid Steering vs. Explicit Steering for a Wheeled Mobile Robot", M.S Thesis in Robotics, Carnegie Mellon University, 1999.
13. H. Oravec, V. Asnani, and X. Zeng, "Design and characterization of GRC-1: A soil for lunar terramechanics testing in Earth-ambient conditions", *Journal of Terramechanics*, Vol. 47, No. 6, 2010, pp. 361-377.
14. C. Creager, V. Asnani, H. Oravec, and A. Woodward, "Drawbar Pull (DP) Procedures for Off-Road Vehicle Testing", NASA Technical Report, August, 2017.
15. G. Ishigami, A. Miwa, K. Nagatani, and K. Yoshida, "Terramechanics-Based Model for Steering Maneuver of Planetary Exploration Rovers on Loose Soil", *Journal of Field Robotics*, Vol. 24, No. 3, 2007, pp. 233-250.
16. K. Skonieczny, "Modeling the effects of surcharge accumulation on terrestrial and planetary wide-blade soiltillage tool interactions", *Soil & Tillage Research*, Vol. 176, 2018, pp. 104-111.